

TAXONOMY AND LIGHT-CURVE DATA OF 1000 SERENDIPITOUSLY OBSERVED MAIN-BELT ASTEROIDS

N. ERASMUS,¹ A. MCNEILL,² M. MOMMERT,^{3,2} D. E. TRILLING,^{2,1} A. A. SICKAFOOSE,^{1,4} AND C. VAN GEND¹

¹*South African Astronomical Observatory, Cape Town, 7925, South Africa.*

²*Department of Physics and Astronomy, Northern Arizona University, Flagstaff, AZ 86001, USA.*

³*Lowell Observatory, Flagstaff, AZ 86001, USA.*

⁴*Department of Earth, Atmospheric, and Planetary Sciences, Massachusetts Institute of Technology, Cambridge, MA 02139-4307, USA.*

ABSTRACT

We present *VRI* spectrophotometry of 1003 Main-Belt Asteroids (MBAs) observed with the Sutherland, South Africa, node of the Korea Microlensing Telescope Network (KMTNet). All of the observed MBAs were serendipitously captured in KMTNet’s large $2^\circ \times 2^\circ$ field of view during a separate targeted near-Earth Asteroid study (Erasmus et al. 2017). Our broadband spectrophotometry is reliable enough to distinguish among four asteroid taxonomies and we confidently categorize 836 of the 1003 observed targets as either a S-, C-, X-, or D-type asteroid by means of a Machine Learning (ML) algorithm approach. Our data show that the ratio between S-type MBAs and (C+X+D)-type MBAs, with H magnitudes between 12 and 18 ($12 \text{ km} \gtrsim \text{diameter} \gtrsim 0.75 \text{ km}$), is almost exactly 1:1. Additionally, we report 0.5- to 3-hour (median: 1.3-hour) light-curve data for each MBA and we resolve the complete rotation periods and amplitudes for 59 targets. Two out of the 59 targets have rotation periods potentially below the theoretical zero cohesion boundary limit of 2.2 hours. We report lower limits for the rotation periods and amplitudes for the remaining targets. Using the resolved and unresolved light curves we determine the shape distribution for this population using a Monte Carlo simulation. Our model suggests a population with an average elongation $b/a = 0.74 \pm 0.07$ and also shows that this is independent of asteroid size and taxonomy.

Keywords: minor planets, asteroids: individual (Main-Belt Asteroids) — techniques: photometric — surveys

1. INTRODUCTION

Main-Belt Asteroids (MBAs) are the most abundant designated objects in the Solar System, representing approximately 95% of all bodies listed in the Minor Planet Center (MPC)¹ catalog. There are estimated to be 1×10^6 asteroids in the main belt with a diameter larger than 1 km (Bottke et al. 2005). In this work we present a series of spectrophotometric light curves, both partial and full, for around 1000 MBAs of comparable diameter. In principle, this work is a successor to the Thousand Asteroid Light Curve Survey (Masiero et al. 2009) but with simultaneous taxonomy determination included. Similar to Masiero et al. (2009), by conducting an untargeted survey we have obtained photometry for a sample of MBAs that will be unbiased against objects with low-amplitude light curves or long rotation periods.

Photometric data is the most abundant data available for minor planets and through analysis of this it is possible to gain insight into the rotational behavior and shape properties of asteroids. The Asteroid Light Curve Database (LCDB; Warner et al. 2009, Updated 2017 September 11)² contains 16,837 MBA light curves with 3201 having accurately determined and unambiguous rotation periods. With sufficient observations at multiple observing geometries it is possible to estimate the shape and spin pole of the objects by light curve inversion (Kaasalainen & Torppa 2001). With sparse photometry or partial light curves this is much more difficult. Instead, statistical models are often used to determine the shape distribution of a population as a whole where sparse photometry is available, rather than attempting to determine the shape properties of an individual object. Previous work on this topic was carried out in McNeill et al. (2016) and Cibulková et al. (2017).

Asteroid composition can be remotely probed with spectroscopy. The reflected light spectrum of an asteroid can be compared to the reflectance spectra of known collected meteorite types and in this way the composition of asteroids can be inferred. The most widely used spectral system is the Bus-DeMeo taxonomic scheme (DeMeo et al. 2009) consisting of 24 spectral types and sub-types that are defined in the wavelength range of 0.45–2.45 μm . Although there are many Bus-DeMeo taxonomic classes, MBAs fall mainly in two groups: silicon-rich asteroids with a distinct spectral feature, which are classified as S-type asteroids, and those that have featureless flat or reddish spectral slopes in the visible region, which could be one of several classes. Asteroids with featureless spectra are most commonly C-type (carbonaceous) asteroids, but also include X-type (several different possible compositions) asteroids, and lastly D-type (even more primitive material) asteroids.

In some cases spectrophotometry where the reflectance spectra of an asteroid is sampled at strategic wavelengths using broadband filters is adequate to determine the spectral. Therefore spectrophotometry can not ascertain asteroid composition but still has the ability to distinguish between some of the taxonomic classes. For instance, *VRI* spectrophotometry in the visible region is sufficient to distinguish between spectral slopes of S-, X- and C- and D-type Bus-DeMeo taxonomic classes (Erasmus et al. 2017). This is the method used in this study to determine each MBA’s likely taxonomy. Spectrophotometry has the benefit of being employable to investigate fainter asteroids. This significantly increases the observable population numbers since the size distribution is heavily skewed towards smaller asteroids.

Here we present *VRI* spectrophotometry observations and 0.5- to 3-hour light-curve data for 1003 MBAs. In Section 2 the observational details, the method for extracting serendipitously observed MBAs, and the photometry pipeline are explained. In Section 3 the photometric results of the 1003 observed MBAs are presented. Section 4 describes how the color, classification, and light curve of each MBA was determined from the photometric data. In Section 5 we give detail on the shape-modeling procedure. Sections 6 and 7 conclude this study by discussing the analyzed data and the derived shape distribution, comparing to other published work, and presenting our conclusions.

2. OBSERVATIONS AND DATA REDUCTION

Observations were made with the Sutherland, South Africa, node of the Korea Microlensing Telescope Network (KMTNet) (Kim et al. 2016). The telescope has a primary mirror 1.6 m in diameter and is fitted with four 9k \times 9k CCDs, mosaicking the $2^\circ \times 2^\circ$ field of view. Each CCD covers $1^\circ \times 1^\circ$ of sky with a plate-scale of 0.40 arcsec/pixel. Observations were performed alternating among *V* ($\lambda = 550$ nm, $\Delta\lambda = 90$ nm), *R* ($\lambda = 660$ nm, $\Delta\lambda = 140$ nm), and *I* ($\lambda = 805$ nm, $\Delta\lambda = 150$ nm) filters in the sequence *VRVI*, repeating the sequence continuously for the entire observing

¹ <http://minorplanetcenter.net/>

² <http://www.MinorPlanet.info/lightcurvedatabase.html>

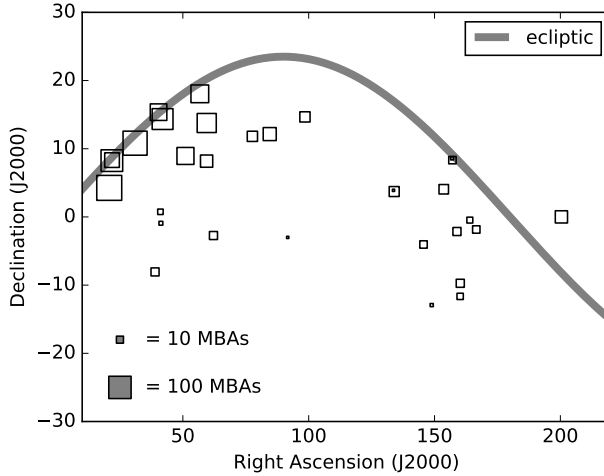


Figure 1. Sky-coordinates of all observed KMTNet fields used in this study (hollow squares). The size of the square is proportional to the number of serendipitous MBAs with acceptable SNR extracted in each field. As expected, fields observed on or close to the ecliptic yielded the highest number of MBAs, though some fields on the ecliptic only yielded a few MBAs because unfavorable observing conditions for that specific field meant a large number of MBAs had to be discarded.

duration. The exposure time for each filter was 60 seconds, which limited this study to MBAs with magnitudes $V \lesssim 21$ to achieve the desired signal-to-noise ratio (SNR) of at least 10 in a single exposure.

Observations were originally performed for a near-Earth asteroid study that took place between 25 October 2016 – 20 February 2017 over four observing weeks (Erasmus et al. 2017). However, the large field of view of KMTNet meant that the 31 fields observed in that study also included many serendipitously observed MBAs. The squares in Figure 1 show the location of the 31 observed fields with the size of the square proportional to the number of MBAs extracted from each field.

To extract all serendipitously observed MBAs in the observed fields, the ephemerides for all $\sim 700,000$ known asteroids in the MPC’s database were calculated at the respective mid-time of each observation. Ephemerides were calculated using PyEphem³ and any MBA falling within the observed field’s coordinate perimeter was flagged. Flagged asteroids were queried with JPL’s Horizons service⁴ using the Python module CALLHORIZONS⁵ and discarded if $V > 21$. In total ~ 2000 serendipitous MBAs were captured and 1003 of them produced spectrophotometry data with acceptable data quality ($\text{SNR} \geq 10$ in all bands).

Photometry and light-curve extraction was achieved using PHOTOMETRYPIPELINE (PP) developed by Mommert (2017). The pipeline utilizes the widely used Source Extractor software (Bertin & Arnouts 1996) for source identification and aperture photometry. SCAMP (Bertin 2006) is used for image registration. Both image registration and photometric calibration are based on matching field stars with star catalogs from the Sloan Digital Sky Survey, the AAVSO Photometric All-Sky Survey, Pan-STARRS, and GAIA.

3. RESULTS

Figure 2 shows the photometric data for nine of the 1003 observed MBAs (see the electronic edition of Figure 2 for all observed MBAs. For reviewer: see attached zipped file). We show the calibrated photometric results generated by PP from the V -, R -, and I -filter images. Adjusted R and I data are also shown (inter-spaced between V data), which results in a final light curve (bottom set of data in each plot). Sections 4.1 & 4.3 describe details of the process for adjusting the R and I data points. Photometric uncertainties account for instrumental uncertainties as well as statistical uncertainties when compared to the photometric catalog.

³ <https://github.com/brandon-rhodes/pyephem>

⁴ <https://ssd.jpl.nasa.gov/horizons.cgi>

⁵ <https://github.com/mommertmi/callhorizons>

For a single exposure a SNR of 30–40 was achieved for targets with $V \approx 18$ and around 10 for $V \approx 21$. A SNR of 10 in a single exposure with a median observation duration of 1.3 hours yielded an error in calculated color of less than 0.1 magnitude.

For each image the PP also outputs cropped thumbnail images centered around the predicted position of the target. The aperture size and aperture position is also indicated. These thumbnail images were visually inspected for all outlying data points. Data points were manually deleted where in the corresponding image it was clear that the wrong source was selected, or that the target intersected a CCD defect or a star.

4. ANALYSIS

In this section we discuss how the colors, taxonomy, and rotational parameters for each observed MBA were determined. The results from this analysis are summarized in Table 1.

4.1. Colors

The $V-R$ and $V-I$ colors of each MBA are calculated by simply subtracting the calibrated I and R magnitudes from the V magnitude. To account for variations in magnitude due to rotation, a linear interpolation was performed between adjacent V data points. The interpolation was used to obtain a corrected V magnitude at times of inter-spaced non- V observations. Respective colors were derived by subtracting the non- V magnitudes from these interpolated V magnitudes. The final color is the weighted average (by error in respective data points) of all retrievable subtraction calculations in an observation and is shown in the top-right of each plot in Figure 2. The final colors were also corrected for solar colors by subtracting the respective $V-R = 0.41$ and $V-I = 0.75$ solar colors (Binney & Merrifield 1998). The solar corrected colors of all observed MBAs are shown in Table 1 and plotted in Figure 3 (b).

4.2. Taxonomic Classification

To classify each observed MBA as one of S-, X-, C- or D-type asteroid, a Machine Learning (ML) algorithm approach was employed as described by Mommert et al. (2016). The ML algorithm was trained using asteroid colors that were synthesized from measured asteroid spectra taken from the MIT-UH-IRTF Joint Campaign for NEO Spectral Reconnaissance⁶. The spectra were classified using the Bus-DeMeo taxonomy spectrum classification online routine⁷ and in the end 74, 34, 28 and 6 reliable $V-R$ and $V-I$ colors of S-, X-, C- and D-type asteroids, respectively, were synthesized. Mommert et al. (2016) provides more detail on generating training data for the ML algorithm.

The synthesized colors (training data) are plotted and shown in Figure 3 (a) and the resultant classification boundaries generated by the ML algorithm are also indicated. The training of the ML algorithm was executed using the `scikit-learn` module (Pedregosa et al. 2011) for Python. The k-nearest neighbor (k=5) method was implemented, as in Mommert et al. (2016) and Erasmus et al. (2017).

In order to account for uncertainties in the measurement of each MBA’s color, a Monte-Carlo approach was used where 10^4 pseudo-measured colors were randomly generated with a Gaussian distribution within the corresponding 1σ uncertainties of each MBA’s real measured color (see Erasmus et al. (2017) for example plots illustrating this process). Each of the 10^4 instances of each MBA was classified using the trained ML algorithm (i.e., where they are located relative to the decision boundaries) and the overall frequency of each taxonomic type was tallied. The classification probability for each taxonomic type was then calculated. The most likely (i.e., highest probability) taxonomic type was assigned to the MBA only if this probability was larger than 50% (see Table 1 for probabilities and the symbol in adjacent column which indicates the most likely classification). The assigned classifications are indicated in Figure 3 (b) by means of the color of the data point (orange = S-type, blue = X-type, pink = C-type, yellow = D-type asteroid and black = undetermined).

4.3. Light Curves

Light curves were produced by combining the V magnitude data points with adjusted I and R magnitude data points. Adjustments were implemented by normalizing the original I and R magnitude data points to V magnitudes by adding the derived colors (see Section 4.1 for detail on how colors were derived). Examples of resultant light curves are shown as the bottom curves in Figure 2 (a)-(i) with the original V data and adjusted R and I data inter-spaced.

⁶ <http://smass.mit.edu/minus.html>

⁷ <http://smass.mit.edu/busdemeoclass.html>

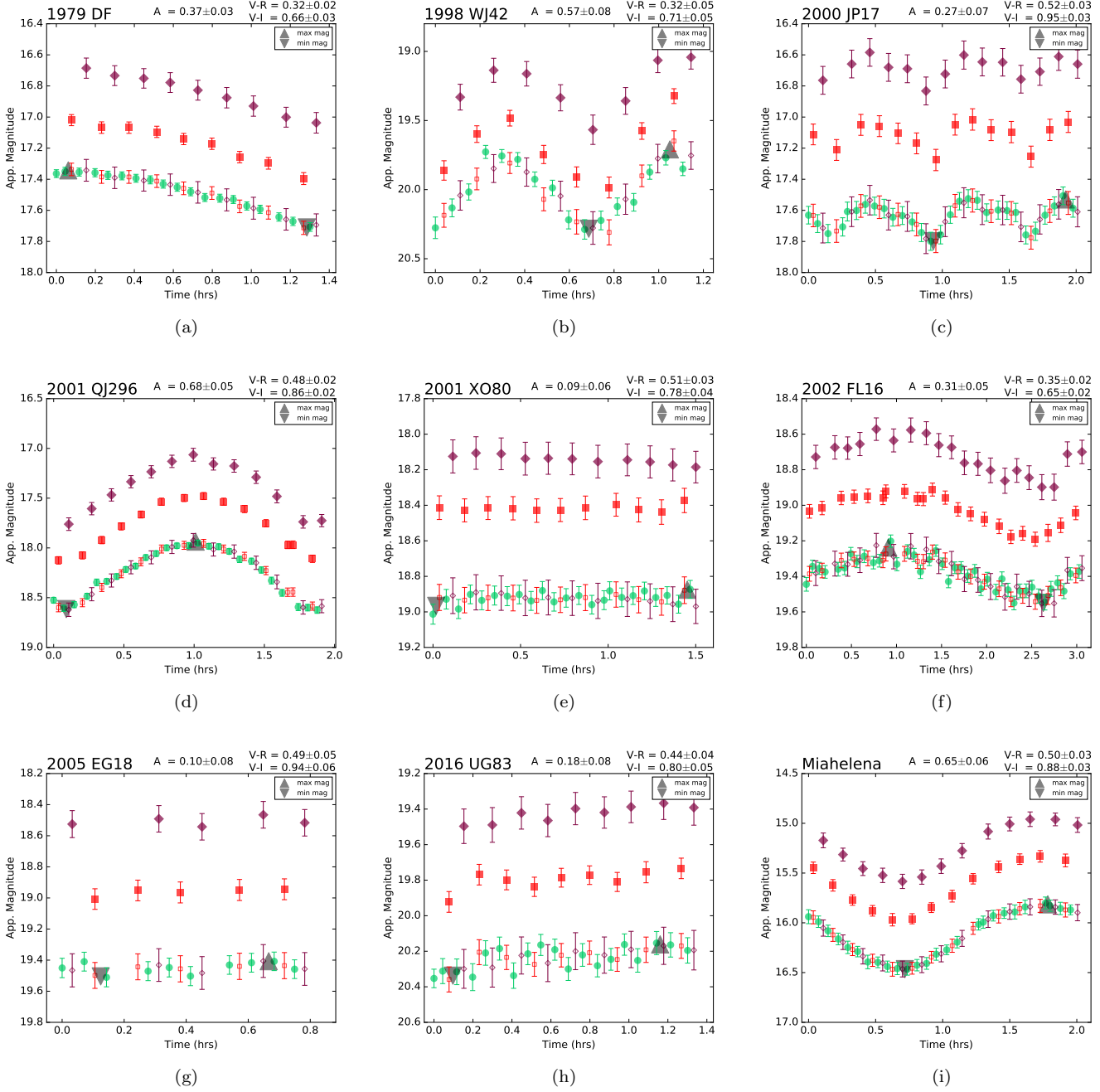


Figure 2. Example photometric data for nine of the observed MBAs. The data are the calibrated photometric results generated by PP developed by Mommert (2017). The V - (green circles), R - (red squares), and I - (burgundy diamonds) filter data are shown. A final light curve (bottom set of data in each plot) is constructed by offsetting R and I data with a constant value (see Section 4.1 and 4.3). The adjusted data points are displayed as smaller, hollow symbols interspersed with the V data. The lower limit on the amplitude (A) is calculated using the difference between magnitudes highlighted with the gray triangle symbols. The triangles are situated where the mean of two adjacent data points have the minimum/maximum magnitude. See the electronic version for all 1003 plots. (For reviewer: see attached zipped file)

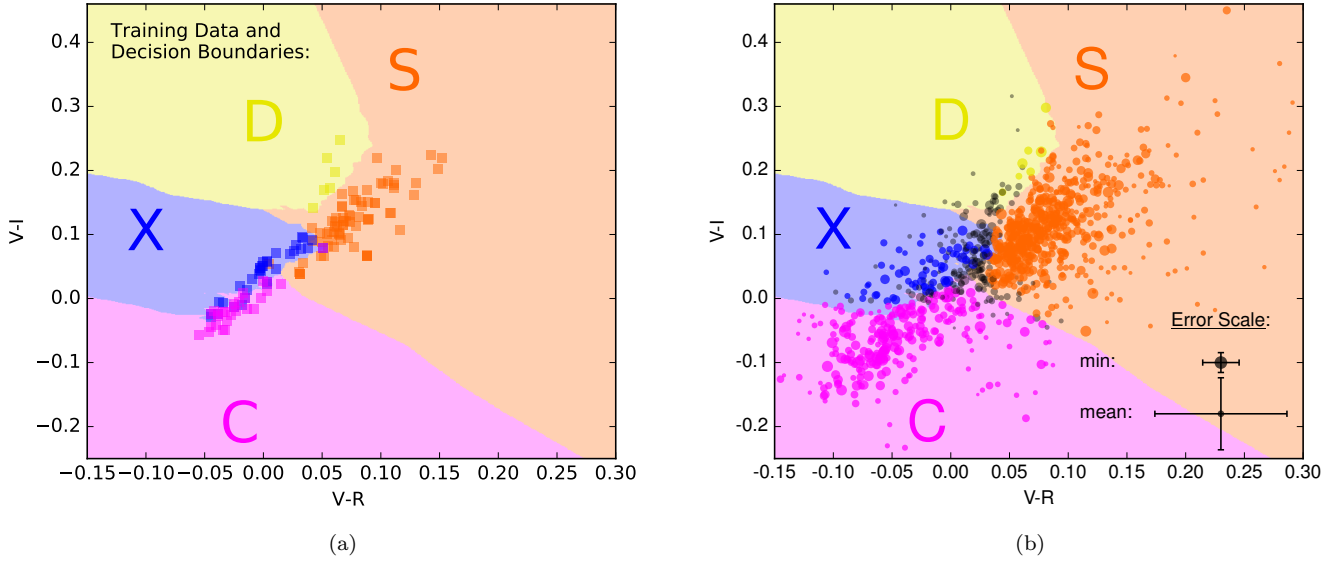


Figure 3. (a) The training data synthesized from MIT-UH-IRTF spectra (see Section 4.2) and resultant decision boundaries generated by the ML algorithm. (b) The calculated colors of all observed MBAs (see Section 4.1 for detail) with the decision boundaries superimposed. MBAs in orange, blue, pink and yellow were classified by the ML algorithm (see Section 4.2) as S-, X- and C-type asteroids, respectively. MBAs in black remain unclassified since the highest taxonomic probability was less than 50%. Sizes of the data points are inversely proportional to the uncertainty (scale is shown). The probabilities (see Section 4.2) for each type are given in Table 1.

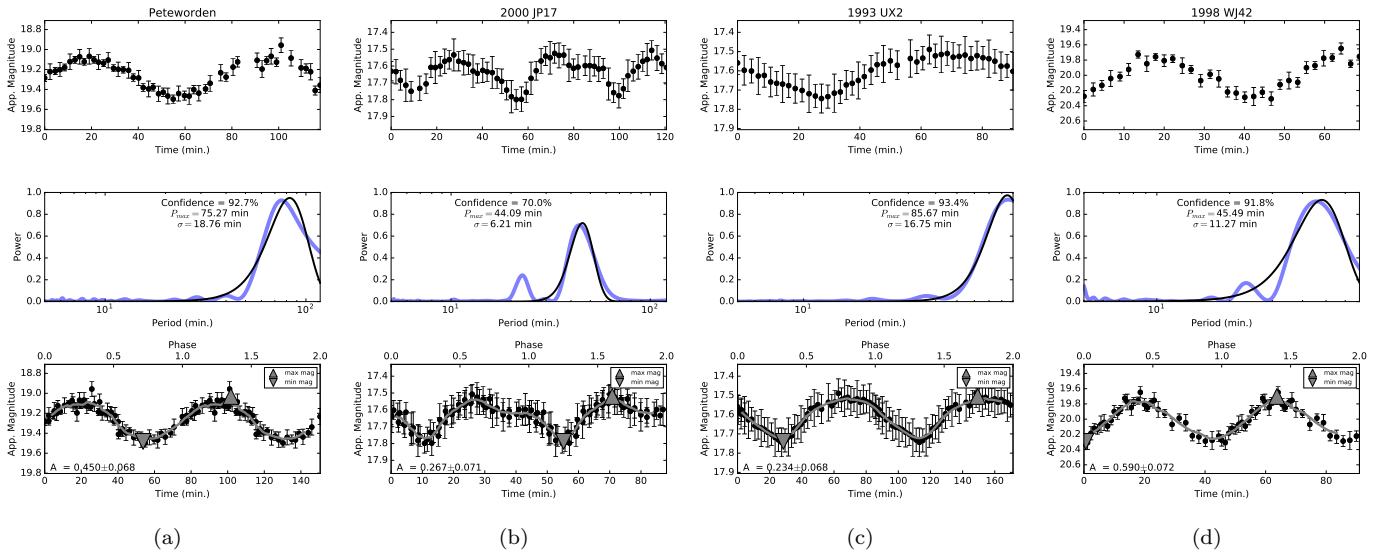


Figure 4. Top plots: combined V , R and I calibrated photometric data of four observed MBAs producing a light curve. The periodogram of the light-curve data and folded representation of the original light-curve data are shown underneath each light-curve plot. P_{max} is used as the folding interval. The bottom plots show folded data spanning two of the best-fit light-curve periods. The amplitude (A) is displayed with gray triangles, situated where the mean of two adjacent data points have the minimum/maximum value, indicating the values used for determining A . See the electronic edition for data for all 59 MBAs that produced periodograms with a distinct peak. (For reviewer: see attached zipped file).

The majority of the light curves only cover a fraction of the rotational period (e.g., 1979 DF in Figure 2 (a)), and therefore in most cases only lower limits on both the light curve amplitude and asteroid rotation period could be reported in Table 1. However, we performed a least-squares spectral analysis (Lomb-Scargle, Lomb 1976; Scargle 1982) on all the light curves to estimate a frequency spectrum and thereby generate a periodogram of each observed MBA. Any observed MBA with a periodogram peak with a confidence larger than 60% was flagged as a potentially resolved light curve. After manual inspection, 59 observations were identified as potentially resolved light curves. Four examples are shown in Figure 4.

The uncertainty of this periodicity is determined by fitting a Gaussian function to the periodogram peak and using the RMS width (σ) as the uncertainty (see superimposed black curve and σ of the fitted function). The light-curve period P_{max} and the confidence in the periodogram peak is also indicated on the plot. The bottom set of plots in Figure 4 show the folded representation of the original light-curve data using P_{max} as the folding interval. Using this folded data, the amplitude is calculated using the difference between magnitudes highlighted with the gray triangle symbols. The triangles are situated where the mean of two adjacent data points have the minimum/maximum magnitude. The asteroid rotation period (i.e., double the light-curve period obtained from the periodogram peak position) and the amplitudes determined from the folded data are listed in Table 1 for the 59 targets. For the remaining targets the lower limit of the rotation period (i.e., the observational duration) and the lower limit of the amplitude are used to complete Table 1. In the latter case, the amplitude lower limited is calculated in the same way as before but instead the original unfolded data are used (see gray triangles in Figure 2).

5. SHAPE-DISTRIBUTION MODELING

To obtain an estimate of the shape distribution of our MBA population we use an improved form of the model described in McNeill et al. (2016). This model generates a synthetic population of ellipsoidal asteroids with assumed shapes and spin-pole orientations. We assume a uniform spin frequency distribution, corresponding to rotational periods between 2.2 and 24 hours, across all applicable size ranges comparable to the uniform distribution of rotational frequencies at the size range present in our dataset (Pravec et al. 2002). The synthetic population is sampled using the same cadence as the KMTNet observations and for time-spans consistent with the lengths of the partial light curves measured. The model also assumes an uncertainty on each measurement based on the distribution of uncertainties in the measured magnitudes from the data. It is important to note that the magnitudes generated by the model are assumed purely to be due to geometric effects i.e., limb-scattering effects and albedo variance are not accounted for.

Using the model described above we determined the best-fit shape distribution to the observed data. To quantitatively determine the goodness of the fit for each model population we employ the two-sampled chi-squared test and seek the best fit by minimizing this value. Assuming that all asteroids are prolate spheroids ($a > b = c$) the value of b/a was varied as a truncated Gaussian with a centre μ and standard deviation σ . The Gaussian distribution was truncated at the point where $b/a = 1$. The spin-pole distribution of the populations was also varied between a distribution in which all objects are aligned with the orbital plane and a distribution where the spin-pole axes are randomly oriented. For each shape and spin-pole configuration the population is sampled using the same cadence as our observations in order to obtain the best possible fit to the measured partial light curves. We obtained valid fits of different shape distributions across all possible spin distributions considered so we are unable to determine any information about the spin distribution of the objects in our sample.

6. DISCUSSION

6.1. Taxonomic Distribution

Figure 5 shows the taxonomic distribution of all our observed MBAs as a function of H magnitude. Panel (a) gives a broad overview of the distribution and is based on the discrete classification, i.e., only the highest classification probability, as in Figure 3 (b), is used to assign a taxonomy to each MBA. Panel (b) shows the distribution in three H magnitude bins and in this case the distribution is obtained by summation of the probability fractions in Table 1 for each respective class type. The plots suggest that the ratio between S-type MBAs and (C+X+D)-type MBAs with H magnitudes between 12 and 18 ($12 \text{ km} \gtrsim D \gtrsim 0.75 \text{ km}$) is within uncertainties almost exactly 1:1 with perhaps a slight decrease in S-type asteroids for the larger MBAs in our size range.

To determine if any correlation exists between asteroid taxonomy and orbital parameters we performed Spearman correlation tests between our determined taxonomic class probability and three orbital parameters: semi-major axis, eccentricity and inclination. The only significant correlation the tests revealed was between semi-major axis and the

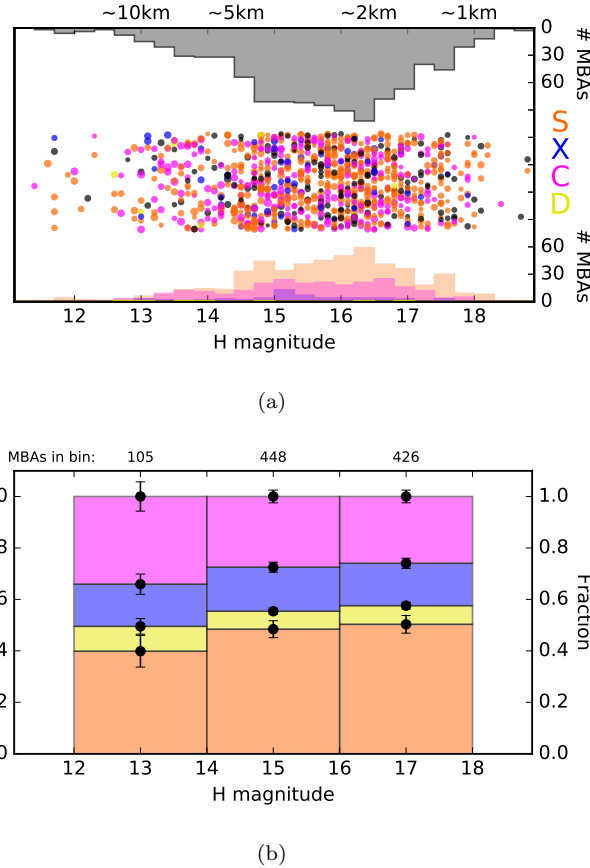


Figure 5. (a) Taxonomic distribution as a function of H magnitude. Note that the data point colors and plotted histograms are based on discrete classification i.e., only the highest classification probability in Table 1 is considered. MBA size estimations (assuming an albedo of 0.12) are also indicated. (b) The distribution in three H -magnitude bins. Here the calculated fractions for each taxonomy are based on the summation of the probabilities in Table 1 for each respective class type.

probability of an MBA being a S- or C-type. This correlation can also be seen in Figure 6 where we show the taxonomic distribution of all our observed MBAs as a function of semi-major axis. Panels (a) and (b) show the same data but with inclination and H magnitude the y-axis variable. As in panel (a) of Figure 5 only discrete classification is used here. The histograms show that C-type asteroids are more prevalent in the outer main-belt and S-type asteroids more prevalent in the inner main-belt, which agrees with previously reported findings (Bell et al. 1989; Carvano et al. 2003; DeMeo & Carry 2013). Panel (c) shows the distribution in six semi-major axis ranges (separated by the Kirkwood gaps) and here the trend is clear that the ratio between S-type MBAs and C-type MBAs decreases with increasing heliocentric distance.

We compare our taxonomic distribution result with DeMeo & Carry (2014) which is a summarized amalgamation of many published results on asteroid taxonomies. It should be noted that their distributions are based on mass rather than numbers. However, the densities (Carry 2012) of S-type asteroids ($2 \text{ g/cm}^3 \lesssim \rho \lesssim 3 \text{ g/cm}^3$) and C-type asteroids ($1.3 \text{ g/cm}^3 \lesssim \rho \lesssim 2.9 \text{ g/cm}^3$) are similar enough to make a direct comparison in rough trends permissible. Although their smallest size range (5–20 km) is slightly larger than our size range, their absolute taxonomic distribution ratios and the heliocentric-distance dependence on these ratios appears similar to our results.

We also cross-checked our MBAs with NASA’s Small Bodies Data Ferret database (SBDF) (Nesvorný 2015) which allowed us to assign an asteroid family to roughly one third of our MBAs. In general we found a good agreement with our determined taxonomy and the taxonomy associated with the corresponding asteroid family (Nesvorný et al. 2015).

6.2. Light-Curve Data

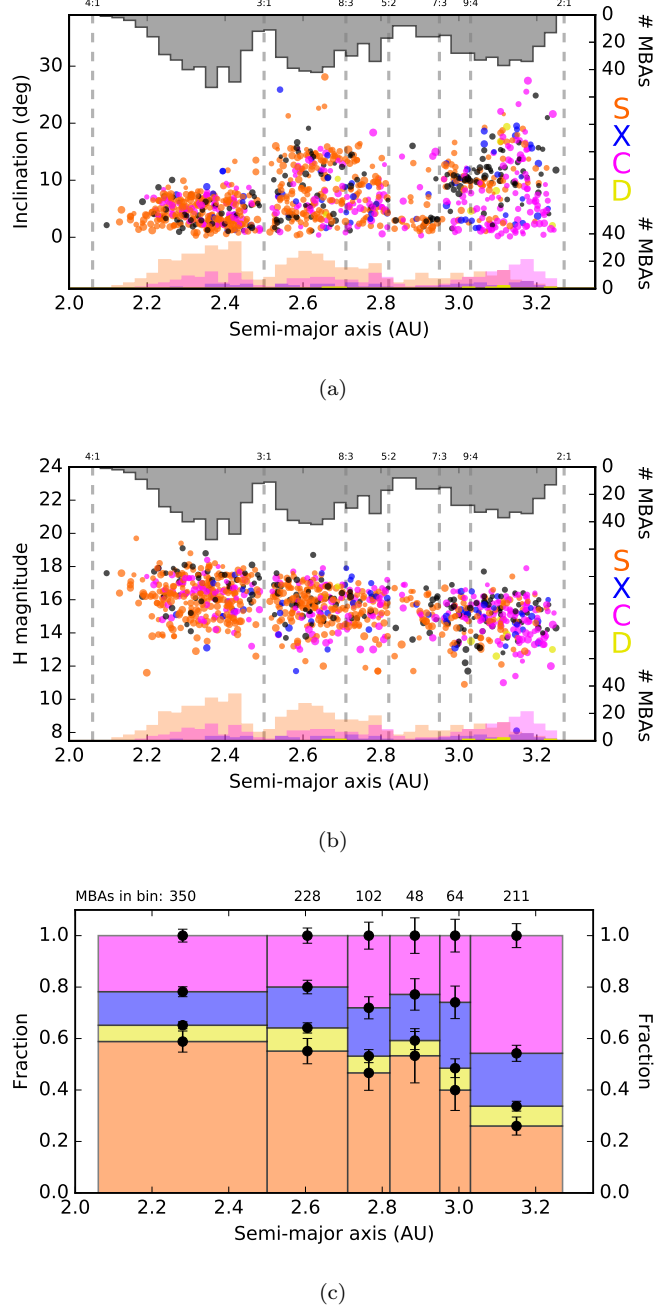


Figure 6. (a) and (b) Taxonomic distribution as a function of semi-major axis with inclination and H magnitude on the y-axis variables respectively. Note that the data point colors and plotted histograms are based on discrete classification i.e., only the highest classification probability in Table 1 is considered. (c) The distribution in six semi-major axis ranges (separated by the Kirkwood gaps, see dotted lines in (a) and (b)). Here the calculated fractions for each taxonomy are based on the summation of the probabilities in Table 1 for each respective class type.

Figure 7 shows rotational periods plotted as a function of MBA size for the 59 targets observed that had potentially resolved light-curve periods (see Section 4.3). The known rotational periods for all asteroids (from the LCDB) are also shown and in most cases our data show similar trends to already reported rotational periods in our size range i.e., most of our MBAs have rotational periods below the theoretical zero cohesion boundary limit of 2.2 hours. However, there are two exceptions, 1998 WJ42 and 2000 JP17 (circled in 7 (b)) that both have light-curves (shown in Figure

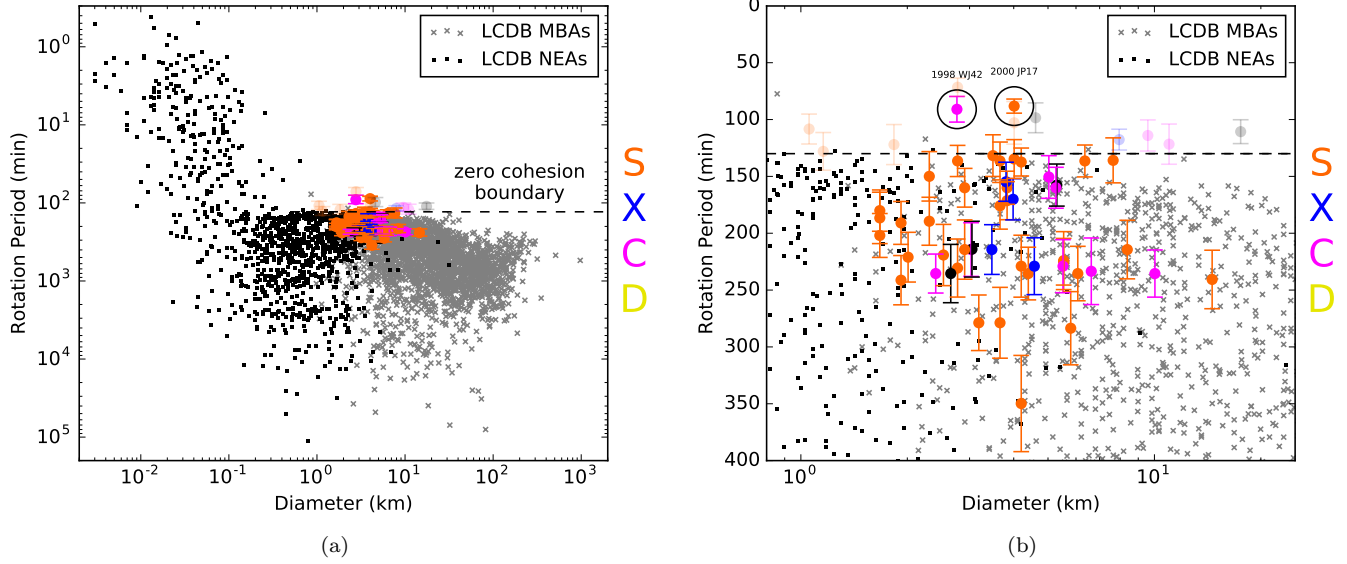


Figure 7. (a) Rotation periods as a function of size of the 59 MBAs observed that had potentially resolved light-curve periods. For the size estimation we use albedos determined by Ryan & Woodward (2010) for the corresponding taxonomy. The LCDB (Warner et al. 2009, updated 2017 September 11) data are also plotted. (b) Zoom-in of panel (a) with the color of the data points showing the assigned taxonomy (see Section 4.2) with orange = S-type, blue = X-type, pink = C-type, yellow = D-type asteroid and black = undetermined. MBAs with a derived rotational period (see Section 4.3) below the theoretical zero cohesion boundary limit of 2.2 hours (dotted line) that had confidence in the periodicity determination below 70%, or where extracted light-curve period was close to the observation duration, are shown as lightly shaded data points because these conditions would mean there are justified doubts on the legitimacy of the calculated period. The light curves and periodograms of the two circled data points are shown in Figure 4 (b) and (d) with both showing fully-resolved rotation-period values suggesting that these two MBAs are potential Super-Fast Rotators (SFRs) for their size.

4 (b) and (d)) displaying rotation periods below the zero cohesion boundary. These two objects could be potential Super-Fast Rotators (SFRs) and further observations to confirm their SFR status are planned.

For the 59 targets we also tested for correlations between determined taxonomic class probability and the two calculated light-curve parameters: rotation period and light-curve amplitude. No statistical significant correlations were found.

6.3. Shape-Distribution Modeling

The result of the shape-distribution modeling and fitting explained in Section 5 is shown in Figure 8. The plot indicates that the best fit for the average measured elongation is $b/a = 0.74 \pm 0.07$. Using the taxonomic classifications determined in this work the shape distributions for both S- and C-type asteroids were calculated. There was no statistically significant difference between the shape distributions obtained for these two classifications, nor was there any difference between these two values and the value obtained for the data-set as a whole. The shape distribution at different size ranges was also generated and no statistically significant difference between the shape distributions was seen.

We compare our shape distribution result with Masiero et al. (2009) which used light-curve data obtained with the Canada-France-Hawaii Telescope (CFHT) and with results obtained by McNeill et al. (2016) and Cibulková et al. (2017), both using Pan-STARRS 1 (PS1) light-curve data with a similar asteroid size range as ours. Masiero et al. (2009) suggest a large contribution from asteroids with $b/a \approx 0.8$. McNeill et al. (2016) find an average axis ratio of $b/a = 0.83 \pm 0.12$ and Cibulková et al. (2017) find $b/a = 0.80$. Therefore, within uncertainties the average axis-ratio values derived in this work are in good agreement with previously published values.

6.4. Duplicate Observations and Comparison to LCDB Values

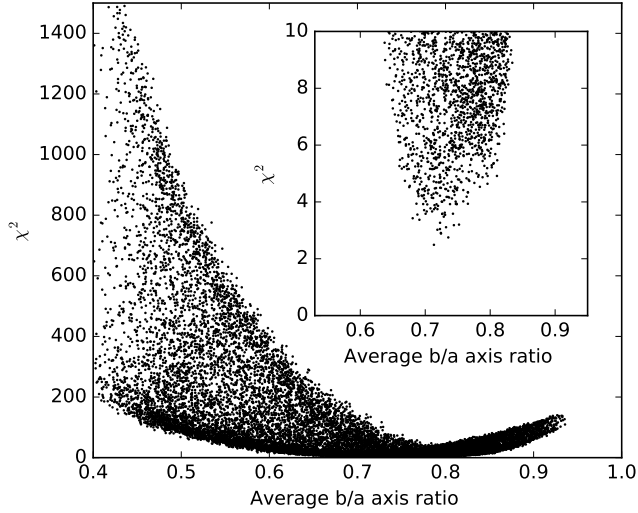


Figure 8. Chi-squared statistics from partial light curves generated from model asteroid populations compared to the observed data. The axis-ratio value corresponds to the mean shape for each model population with a best fit found for $b/a = 0.74 \pm 0.07$ assuming all distributions giving $\chi^2 < 5$ to be valid solutions.

Table 2. Comparison to LCDB values

No.	Object ^a	Amplitude ^b		Rotation Period ^b		Taxonomy ^b	
		this study	(mag)	this study	(minutes)	this study	LCDB
01	2001 PV42	≥ 1.07	-	≥ 106	330.00	S	S
02	Andronikov	≥ 0.29	0.39	≥ 52	189.17	X	S
03	Ara	≥ 0.02	0.34	≥ 58	246.96	X	M
04	Arthuradel	≥ 0.17	0.28	≥ 58	388.56	S	S
05	Billmclaughlin	≥ 0.04	0.07	≥ 37	311.94	X	X
06	Hirayama	≥ 0.21	0.51	≥ 120	937.80	C	C
07	Juliegrady	≥ 0.42	0.90	≥ 114	1128.00	S	S
08	Miahelena	≥ 0.50	0.62	≥ 66	252.06	S	S
09	Miahelena	0.65 ± 0.06	0.62	241 ± 51	252.06	S	S
10	Okabayashi	≥ 0.10	0.10	≥ 53	153.00	S	S
11	Pohjola	≥ 0.12	0.11	≥ 54	175.20	S	S

^aMiahelena appears twice since it was observed twice in this study

^bFirst column are our derived values (see Table 1), second column are the values from the LCDB (Warner et al. 2009, updated 2017 September 11)

There are four MBAs that were by chance observed twice. They are 1981 SU2, 1999 RE190, 2000 UM3 and Miahelena. Within the error bars the derived rotational properties and colors for each instance of the four targets agree. In one case, there was discrepancy between assigned taxonomy. 1999 RE190 was classified as C and X for the two observing datasets but in both instances the calculated color lies in close proximity to a decision boundary generated by the ML algorithm and therefore the probability for the assigned classification is only in the 50% range.

For 1999 RE190 we were also able to resolve the rotation period in both observations. The determined period and amplitude agree within error bars but in both cases the observing duration was very close to the derived light-curve period so there is some doubt if this is the true rotation period. The rotation period and amplitude could only be determined in one of the observations for 1981 SU2 and Miahelena. In both cases the determined values are above the lower limit for the undetermined observation.

Table 2 shows the derived rotational properties and taxonomic classification of all our observed MBAs that were also present in the LCDB (Warner et al. 2009, updated 2017 September 11). In total there were ten MBAs present in both our dataset and in the LCDB. In general we see excellent agreement in both taxonomy and rotational properties.

7. CONCLUSIONS

The *VRI* spectrophotometric results of 1003 MBAs observed with the Sutherland, South Africa, node of KMTNet have been presented. Our broadband spectrophotometry in combination with a ML algorithm allowed us to classify 836 of the 1003 observed target as either a S-, C-, X-, or D-type asteroid. Our data suggest that the ratio between S-type MBAs and (C+X+D)-type MBAs with H magnitudes between 12 and 18 is 1:1, with no discernible H magnitude dependency within the range. This ratio is in agreement with previously published survey studies (DeMeo & Carry 2014). Our results show that the ratio is however dependent on the location within the main-belt with the ratio between S-type MBAs and C-type MBAs decreasing with increasing heliocentric distance. This is also in agreement with previously published survey studies (Bell et al. 1989; Carvano et al. 2003; DeMeo & Carry 2013).

Our light-curve data for each observed MBA allowed us to place lower-limit constraints on the rotational periods and light-curve amplitudes of \sim 950 MBAs and resolve the rotational periods and light-curve amplitudes for 59 MBAs. The lower-limit amplitudes together with the resolved amplitudes allowed us to determine the best-fit shape distribution to the observed data and the average measured elongation is $b/a = 0.74 \pm 0.07$. For the 59 MBAs with resolvable periods our data are also consistent with previously published observations of MBAs with similar sizes with the exception of two targets. 1998 WJ42 and 2000 JP17 display rotation periods below the zero cohesion boundary, suggesting that these are potential Super-Fast Rotators (SFRs) for their size. These two targets require further investigation.

In total there were ten MBAs present in both our dataset and in the LCDB (Warner et al. 2009, updated 2017 September 11). In general we see excellent agreement in both taxonomy and rotational properties.

In the future we plan to continue with the work presented here but will increase our observational duration for each observing field in the hopes of resolving the rotation period for a higher fraction of our targets.

This research has made use of the KMTNet system operated by the Korea Astronomy and Space Science Institute (KASI) and the data were obtained by observations made at the South African Astronomical Observatory (SAAO). This work is partially supported by the South African National Research Foundation (NRF). This work is supported in part by the National Aeronautics and Space Administration (NASA) under grant No. NNX15AE90G issued through the SSO Near-Earth Object Observations Program and in part by a grant from NASA's Office of the Chief Technologist.

REFERENCES

- Bell, J., Davis, D., Hartmann, W., & Gaffey, M. 1989, in Asteroids II, ed. R. Binzel, T. Gehrels, & M. Matthews, 921–945
- Bertin, E. 2006, Astronomical Data Analysis Software and Systems XV, 351, 112
- Bertin, E., & Arnouts, S. 1996, *Astronomy and Astrophysics Supplement Series*, 117, 393
- Binney, J., & Merrifield, M. 1998, *Galactic Astronomy*
- Bottke, W. F., Durda, D. D., Nesvorný, D., et al. 2005, *Icarus*, 175, 111
- Carry, B. 2012, *Planetary and Space Science*, 73, 98
- Carvano, J., Mothé-Diniz, T., & Lazzaro, D. 2003, *Icarus*, 161, 356
- Cibulková, H., Nortunen, H., Durech, J., et al. 2017, *Astronomy & Astrophysics*, 1
- DeMeo, F., & Carry, B. 2013, *Icarus*, 226, 723
- DeMeo, F. E., Binzel, R. P., Slivan, S. M., & Bus, S. J. 2009, *Icarus*, 202, 160
- DeMeo, F. E., & Carry, B. 2014, *Nature*, 505, 629

- Erasmus, N., Mommert, M., Trilling, D. E., et al. 2017, *The Astronomical Journal*, 154, 162
- Kaasalainen, M., & Torppa, J. 2001, *Icarus*, 153, 24
- Kim, S. L., Lee, C. U., Park, B. G., et al. 2016, *Journal of the Korean Astronomical Society*, 49, 37
- Lomb, N. R. 1976, *Astrophysics and Space Science*, 39, 447
- Masiero, J., Jedicke, R., urech, J., et al. 2009, *Icarus*, 204, 145
- McNeill, A., Fitzsimmons, A., Jedicke, R., et al. 2016, *Monthly Notices of the Royal Astronomical Society*, 459, 2964
- Mommert, M. 2017, *Astronomy and Computing*, doi:10.1016/j.ascom.2016.11.002
- Mommert, M., Trilling, D. E., Borth, D., et al. 2016, *The Astronomical Journal*, 151, 98
- Nesvorný, D. 2015, *NASA Planetary Data System*, 234, EAR
- Nesvorný, D., Broz, M., & Carruba, V. 2015, arXiv:1502.01628
- Pedregosa, F., Varoquaux, G., Gramfort, A., et al. 2011, *Journal of Machine Learning Research*, 12, 2825
- Pravec, P., Harris, A. W., & Michalowski, T. 2002, *Asteroids III*, 113
- Ryan, E. L., & Woodward, C. E. 2010, *The Astronomical Journal*, 140, 933
- Scargle, J. D. 1982, *Astrophys. J.*, 263, 835
- Warner, B. D., Harris, A. W., & Pravec, P. 2009, *Icarus*, 202, 134

APPENDIX

A. ALL DATA

